JACS
JOURNAL OF THE AMERICAN CHEMICAL SOCIETY
pubs.acs.org/JACS
Article

Inverted Region in Electrochemical Reduction of CO_2 Induced by Potential-Dependent Pauli Repulsion

Leyu Liu and Hai Xiao*

Cite This: https://doi.org/10.1021/jacs.3c02447
Read Online

ABSTRACT: Electrochemical CO_2 reduction reaction (eCO_2RR) is of great significance to energy and environmental engineering, while fundamental questions remain regarding its mechanisms. Herein, we formulate a fundamental understanding of the interplay between the applied potential (U) and kinetics of CO_2 activation in eCO_2RR on Cu surfaces. We find that the nature of the CO_2 activation mechanism in eCO_2RR varies with U, and it is the sequential electron−proton transfer (SEPT) mechanism dominant at the working U but switched to the concerted proton−electron transfer (CPET) mechanism at highly negative U. We then identify that the barrier of the electron-transfer step in the SEPT mechanism exhibits an inverted region as U decreases, which originates from the rapidly rising Pauli repulsion in the physisorption of CO_2 with decreasing U. We further demonstrate catalyst designs that effectively suppress the adverse effect of Pauli repulsion. This fundamental understanding may be general for the electrochemical reduction reactions of closed-shell molecules.

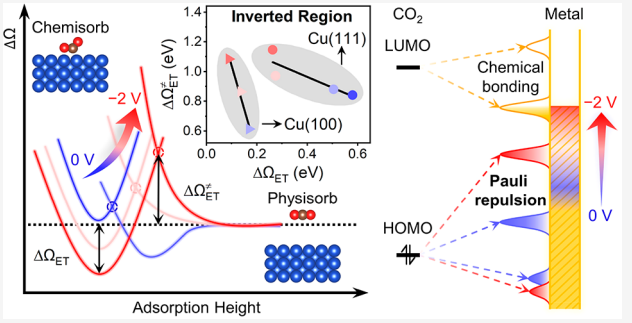

INTRODUCTION

Electrochemical CO_2 reduction reaction (eCO_2RR) powered by renewable energy resources has been envisioned as a promising route to a sustainable and carbon-neutral future.[1,2] To date, Cu-metal-based electrocatalytic systems are still among the best performing for eCO_2RR with a wide spectrum of parameters to tune,[3−10] yet they require further optimization of catalytic performance toward industrial-scale practical applications.[11−13] Therefore, it is of fundamental importance for the rational design of optimal eCO_2RR catalysts to elucidate the atomistic mechanisms of eCO_2RR on Cu-metal-based electrocatalysts, which, however, remains a grand challenge with a variety of contributing factors to explicate.[14−16]

At the very first step of eCO_2RR, i.e., the CO_2 activation, there are exquisite intricacies in its mechanism.[17−19] First, it is demanding to directly activate the inert CO_2 molecule, which is thus coupled with the electron transfer to facilitate the activation to produce the chemisorbed bent CO_2 with a negative charge.[20,21] This leads to two distinctive types of mechanisms for the CO_2 activation in eCO_2RR on Cu:

- One type starts with the electron-transfer (ET) step to activate CO_2 followed by the proton-transfer (PT) step to produce the adsorbed carboxyl (*COOH), and this is the sequential electron−proton transfer (SEPT) mechanism as follows.

$$* + CO_2 + e^- \rightarrow {}^*CO_2^- \text{ (ET)}$$

$${}^*CO_2^- + H_2O \rightarrow {}^*COOH + OH^- \text{ (PT)}$$

- The other combines the ET and PT steps into a single elementary step with a concerted proton−electron transfer (CPET) that activates CO_2 directly to *COOH, and this is the CPET mechanism as follows.

$$* + CO_2 + H_2O + e^- \rightarrow {}^*COOH + OH^- \text{ (CPET)}$$

Note that * represents the active site, and we consider here the neutral condition commonly implemented in eCO_2RR where the solvent H_2O molecule serves as the proton source. Also, there can be variations of these two mechanisms, in which the ET step consumes only a partial charge (δe^-) to produce ${}^*CO_2^{\delta-}$, and the PT step complements the remaining charge of $(1 - \delta)e^-$ to form *COOH with a partial CPET character. Although there have been accumulating studies that shed light on identifying the type of mechanism for the CO_2 activation in eCO_2RR on Cu,[15,22−24] it is not elucidated yet.

Received: March 7, 2023

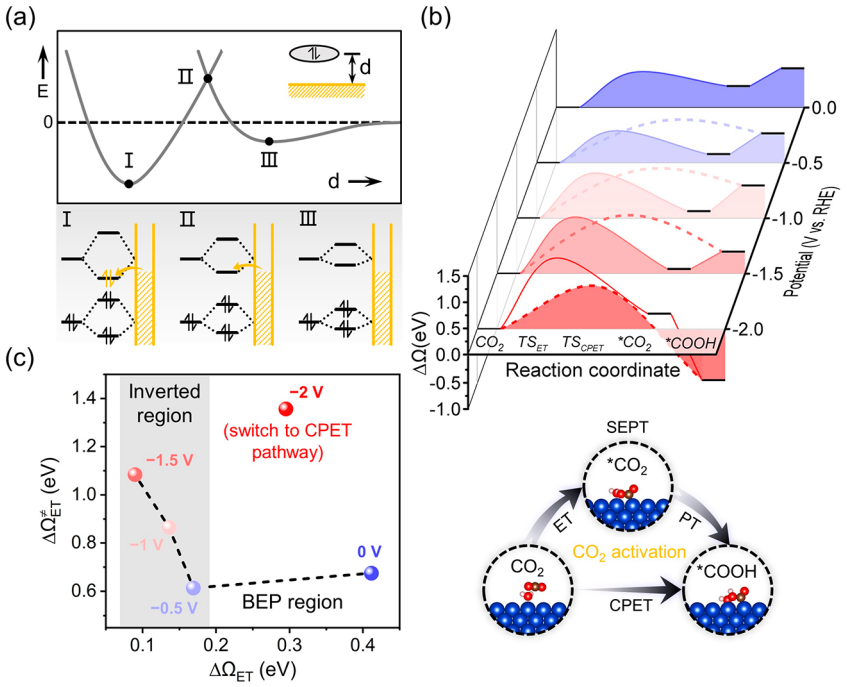

Figure 1. CO_2 activation in eCO_2RR on Cu(100). (a) Schematic illustration of transition from physisorption to chemisorption of a closed-shell molecule approaching a metallic surface, which results in a barrier. (b) Grand free energy profiles of CO_2 activation in eCO_2RR on Cu(100) at U = 0 V, −0.5 V, −1 V, −1.5 V, −2 V (RHE scale at pH = 7) through the SEPT and CPET mechanisms illustrated at the bottom. (c) Correlation between the grand free energy barrier of the ET step ($\Delta\Omega^{\neq}_{ET}$) and the ET reaction free energy ($\Delta\Omega_{ET}$) on Cu(100), which shows a BEP region from 0 V to −0.5 V but a sharply inverted region from −0.5 V to −1.5 V.

A key complication is that, since it is coupled with ET, the CO_2 activation mechanism in eCO_2RR is explicitly dependent on the applied potential (U), and such dependence of its kinetics, particularly the barrier determined by the transition state (TS), is of fundamental interest. In general, a more negative U renders a more negative reaction free energy for the ET or CPET step by the contribution of the eU term, and according to the Brønsted−Evans−Polanyi (BEP) relation that is commonly assumed in heterogeneous catalysis,[25−27] this leads to a lower activation barrier. In the context of electrochemistry, this relation translates to the symmetry factor, which characterizes the fractional charge transfer in the TS and determines the linear dependence of the kinetic barrier on U.[28,29] However, this universal linear relationship may be distorted by the intricate interactions within the electrochemical interfacial region, including the varying responses of relevant species to the charged electrode surface under different U.[30−32]

An even more intriguing question is about the presence of an inverted region predicted by the Marcus theory for both outer and inner sphere ET reactions.[28,33] In the inverted region, the barrier goes higher as the ET reaction energy decreases, and this is in direct contrast to the BEP relation. Nevertheless, on the metallic electrode that has a wide-spreading density of states (DOS) around the Fermi level, the Marcus−Gerischer theory predicts that the inverted region can be ruled out by the continuously available DOS at relevant energy intervals.[34] Therefore, it is plausible to assume the BEP relation for elementary steps of electrochemical reactions on metallic electrodes.

Herein, we employ the grand canonical density functional theory (GC-DFT) method combined with the implicit electrolyte model to explicitly investigate the interplay between the applied potential and the kinetics of CO_2 activation in eCO_2RR on Cu(100) and Cu(111), which serve as ideal model systems for formulating a fundamental understanding that is key to the rational design of optimal catalyst and is thus of practical significance. We first show that the nature of the CO_2 activation mechanism in eCO_2RR varies with U; that is, it is dominated by the SEPT mechanism at the common working U while switched to the CPET mechanism at highly negative U. More strikingly, we then identify inverted regions for the barrier of the ET step in the SEPT mechanism, in direct contradiction with the BEP relation. Thus, the decreasing U raises the barrier for CO_2 activation instead of instilling the thermodynamic driving force into the kinetics. We further elucidate that the inverted region for the barrier, which is determined by the crossing between physisorption and chemisorption potential energy curves, arises from the rapid rising of Pauli repulsion in the physisorption potential energy curve as U decreases. Consequently, we discover designs of electrocatalysts that can effectively diminish the adverse effect of U-dependent Pauli repulsion on the kinetics of CO_2 activation in eCO_2RR.

COMPUTATIONAL DETAILS

To properly describe the van der Waals interactions in the physisorption of CO_2 that is the starting point of CO_2 activation, we first benchmarked a series of DFT exchange−correlation functionals including PBE,[35] PBE-D3,[36] RPBE,[37] RPBE-D3,[36,37] VDW-DF2,[38−41] and BEEF-VDW.[42] Based on the benchmark results listed in Table S1, we chose the PBE-D3 functional, which renders the best agreement with the experimental data for the adsorption energies of CO_2 on Cu surfaces.

https://doi.org/10.1021/jacs.3c02447
J. Am. Chem. Soc. XXXX, XXX, XXX−XXX

All the geometry optimizations and TS searches were performed at explicitly constant electrochemical potentials (μ_e) using the GC-DFT method, together with the charge-asymmetric nonlocally determined local-electric (CANDLE) electrolyte model implemented in JDFTx to describe the electrochemical double layer in a computationally efficient way.[43,44] The implicit CANDLE electrolyte model includes both the solvation effects and the responses of the electrolyte species (cations and anions) to the charged electrode, and the GC-DFT method provides the electron source for charging the electrode at the specified potential. This renders proper distributions of ionic charges in the electrolyte model to mimic the electrochemical double layers at varying potentials. Besides, the implicit CANDLE model can accurately describe the hydrogen bonding and solvation of bare ions in the aqueous electrolyte.[43]

Additionally, we included the interfacial H_2O molecule as the proton source at the neutral condition. Thus, we do not need to use the computational hydrogen electrode (CHE) model to introduce the proton and electron sources.[45] This hybrid combination of implicit electrolyte model and explicit inclusion of relevant solvent molecule has been employed to investigate the eCO_2RR on Cu[46,47] and the oxygen evolution reaction (OER) on (Ni, Fe)OOH,[48] rendering theoretical predictions that match well with the experimental results. The TSs were located at constant potential with the climbing image nudged elastic band (CINEB) method[49,50] implemented in the Atomic Simulation Environment (ASE).[51] We also performed the constrained optimizations at constant potential to obtain the adsorption potential energy curves by scanning the distances between (linear or bent) CO_2 and the Cu surfaces with adaptive step sizes (0.5−2 Å), while we used a much finer scanning step size of 0.01 Å to locate the transition states.

The zero-point energy (ZPE) and free energy corrections including enthalpic and entropic contributions at room temperature (298.15 K) were calculated with the ideal gas approximation and the harmonic approximation for the vibrational modes, and unphysically low-frequency modes were reset to a threshold value of 60 cm^{-1}, which corresponds to the lowest peak frequency (the acoustic translational mode of the six-membered rings) in water bulk.[52,53] More computational details can be found in the Supporting Information (SI).

RESULTS AND DISCUSSION

The CO_2 activation involves the transition from physisorption to chemisorption, which can pose a significant barrier for a closed-shell molecule approaching a metallic surface, and this barrier arises from the crossing of potential energy curves (PECs) for the two states of molecule adsorbed on a surface, i.e., the physisorbed and chemisorbed states, as schematically illustrated in Figure 1a.[54,55] In a simplified picture with only frontier orbitals of the molecule shown in Figure 1a, the repulsive part of the physisorption curve stems from the Pauli repulsion between the highest occupied molecular orbital (HOMO) and the DOS below the Fermi level, while the chemisorption in a reduction scenario does not occur until the lowest unoccupied molecular orbital (LUMO) has sufficiently strong interactions with the empty DOS that render the bonding orbital lower than the Fermi level to accept electrons from the metal.[54] Thus, there is electron transfer between the molecule and surface associated with the transition from physisorption to chemisorption, and this picture can naturally incorporate the coupled ET into the CO_2 activation in eCO_2RR, where the physisorbed and chemisorbed states are sharply distinguished by the linear and bent configurations of CO_2. Therefore, we investigate the grand free energy profiles of CO_2 activation in eCO_2RR on Cu surfaces under varying U, including the key TSs and associated barriers that explicitly take U into account. Note that U is referenced to the reversible hydrogen electrode (RHE) at the neutral condition (pH = 7).

Figure 1b and Figure S1 present the U-dependent grand free energy profiles of CO_2 activation to form the key *COOH intermediate on Cu(100) and Cu(111), respectively. We considered both the SEPT and CPET mechanisms, as illustrated at the bottom of Figure 1b. Note that in both mechanisms the interfacial H_2O molecule gradually changes its orientation and distance with respect to the electrode in response to the varying U (Figure S13), as extensively studied in previous reports,[32,56−58] and the final hydroxyl species is identified as the adsorbed OH^- (Table S4). In the common working range of $U > -1.5$ V, either the grand free energy (Ω) of *COOH or the barrier of the CPET step is higher than the barrier of the ET step on both Cu(100) and Cu(111), and thus the SEPT mechanism kinetically dominates over the CPET mechanism. When U decreases to −1.5 V, the barrier of the CPET step becomes comparable to that of the ET step on both Cu(100) and Cu(111) (Table S2), and at the highly negative U of −2 V, there occurs the drastic change in which the barrier of the CPET step becomes much lower than that of the ET step on both Cu(100) and Cu(111), so the CPET mechanism takes over as the dominant mechanism. Therefore, this evidently demonstrates that the type of mechanism for the CO_2 activation in eCO_2RR varies with U, and it is dominated by the SEPT mechanism at the common working U while switched to the CPET mechanism at highly negative U.

More strikingly, we identify the inverted region in the common working range of U for the ET step in the dominant SEPT mechanism. Figure 1c and Figure S2 plot the grand free energy barrier of the ET step ($\Delta\Omega_{ET}^{\neq}$) against the ET reaction free energy ($\Delta\Omega_{ET}$) at varying U on Cu(100) and Cu(111), respectively. Figure 1c demonstrates that on Cu(100), in the region of U from 0 V to −0.5 V, $\Delta\Omega_{ET}^{\neq}$ and $\Delta\Omega_{ET}$ show a weakly positive linear relationship that conforms to the BEP relation, but in the region of U from −0.5 V to −1.5 V, $\Delta\Omega_{ET}^{\neq}$ increases rapidly as $\Delta\Omega_{ET}$ decreases with U, and this is exactly an inverted region that breaks the BEP relation. On Cu(111), the inverted region spans even wider from 0 V to −1.5 V (Figure S2). At a highly negative U of −2 V, both $\Delta\Omega_{ET}^{\neq}$ and $\Delta\Omega_{ET}$ are elevated, restoring a BEP relation, but $\Delta\Omega_{ET}^{\neq}$ becomes too high and the kinetics favors a dominant CPET mechanism as discussed above (Figures 1b and S1). This arises from the instability of $*CO_2^{\delta-}$ at highly negative U owing to the strong electrostatic repulsion between $*CO_2^{\delta-}$ and the highly negatively charged Cu surface, which can be greatly diminished by the direct formation of *COOH. Note that this strong electrostatic repulsion also leads to the failure of d-band theory in describing the trend of CO_2 chemisorption (Figure S11). Nevertheless, the inverted regions we find on both Cu surfaces are striking, because it indicates that a more negative U, normally a stronger thermodynamic driving force for the ET reduction reaction, exerts a drastically opposite effect on its barrier and kinetics, and this also breaks the common assumption that a catalyst that can chemisorb CO_2 more strongly should deliver a better kinetics. Since the ET step involves the crossing between the PECs of physisorbed and

https://doi.org/10.1021/jacs.3c02447
J. Am. Chem. Soc. XXXX, XXX, XXX−XXX

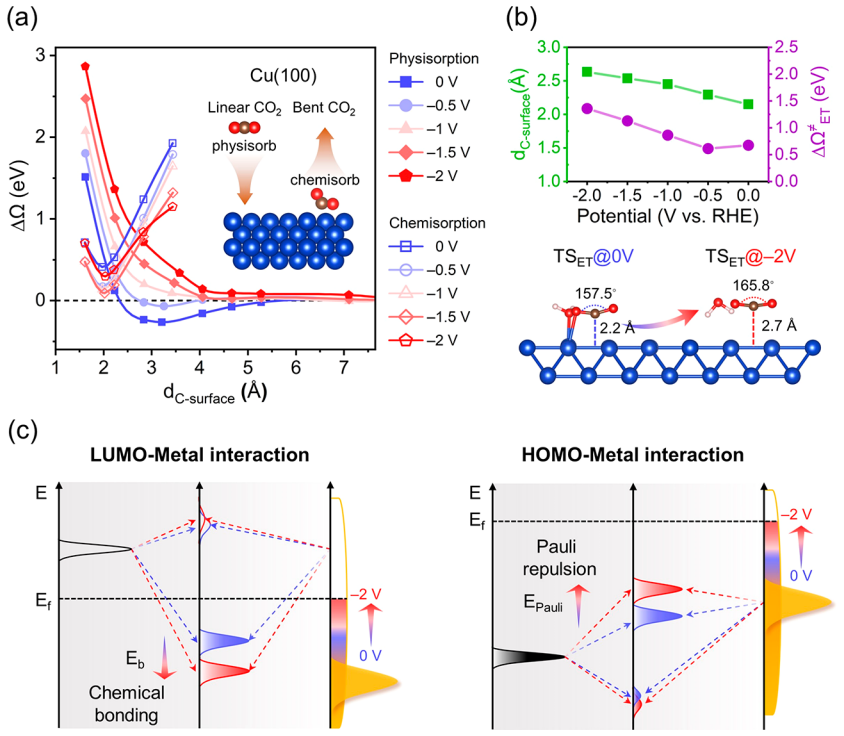

Figure 2. Understanding the origin of the inverted region in the CO_2 activation in eCO_2RR. (a) The potential energy curves of physisorption (linear CO_2) and chemisorption (bent CO_2) on Cu(100) at varying U. (b) The adsorption height of CO_2 ($d_{C\text{-surface}}$) in the TS and the corresponding $\Delta\Omega_{ET}^{\neq}$ on Cu(100) as functions of U from 0 V to −2 V, and the TS structures at 0 V and −2 V are illustrated below. (c) Schematic illustrations of LUMO−metal and HOMO−metal interactions between the CO_2 molecule and Cu surface.

chemisorbed states, we further examine whether the inverted region follows from what Marcus theory depicts.

We adopt the fixed configurations of linear and bent CO_2 taken from corresponding local minima to calculate the U-dependent PECs of physisorption and chemisorption, respectively, as illustrated in Figure 2a for Cu(100) and Figure S3a for Cu(111). At each U, the two PECs cross at the repulsive part of the physisorption PEC that is dictated by Pauli repulsion, and the crossing determines the barrier for the transition. Figure 2a shows that the chemisorption PEC demonstrates a subtle dependence on U; that is, it drops first as U decreases from 0 V to −1.5 V while starts to rise as U further decreases to −2 V. This may arise from the competition between the chemical bonding and electrostatic repulsion between $*CO_2^{\delta-}$ and the negatively charged Cu surface. More significantly, the physisorption PEC rises rapidly and monotonically as U decreases, and this dictates the crossing of two PECs, i.e., the barrier for the transition, to rise rapidly as U decreases. Thus, the inverted region originates from the dominant U-dependence of the physisorption PEC and does not follow from the picture by Marcus theory.

The dominance of physisorption PEC over the barrier is consistent with and also evidenced by the U-dependence of the TS structure of the ET step in the SEPT mechanism (Figure 1b). Figure 2b shows that the CO_2 moiety in this TS becomes further away from the Cu surface as U decreases and resembles more closely the physisorbed state, i.e., a linear CO_2.

Based on the understanding of transition from physisorption to chemisorption shown in Figure 1a, we formulate a qualitative understanding of the U-dependences of the two types of PECs, as illustrated in Figure 2c. When a CO_2 molecule approaches the Cu surface, its doubly degenerate LUMOs and HOMOs (split by the presence of surface) interact strongly with the DOSs of the Cu metal that are energetically close to the LUMOs and HOMOs, respectively, based on the second-order perturbation theory, and this leads to two types of interactions that dictate the chemisorption and physisorption PECs, respectively.

The LUMOs of CO_2 are above the Fermi level and thus interact mainly with the empty DOS of the Cu surface. This type of interaction (labeled as LUMO−metal) leads to bonding orbitals, and their occupations depend on their positions in energy relative to the Fermi level, which are dependent on U. When U decreases, the DOS fills up and the surface becomes more negatively charged, which result in spatially more outward extended band orbitals of surface to increase the overlaps with the LUMOs of CO_2, thus lowering the bonding orbitals. Therefore, the LUMO−metal interactions contribute to the U-dependence of chemical bonding in the chemisorption PEC, although it is complicated by the electrostatic repulsion between $*CO_2^{\delta-}$ and the negatively charged surface as discussed before.

The HOMOs of CO_2, on the other hand, are below the Fermi level and thus interact mainly with the occupied DOS of the Cu surface. This type of interaction (labeled as HOMO−metal) leads to both fully occupied bonding and antibonding orbitals in this scenario, which results in the net Pauli repulsion. This Pauli repulsion is strongly dependent on U: as U decreases, the resulting spatially more outward extended electron density of the surface increases its overlaps with the HOMOs of CO_2, and this elevates the Pauli repulsion rapidly. Note that the CO_2 molecule has high ionization energy, so the antibonding orbitals from the HOMO−metal interactions are unlikely to be pushed above the Fermi level to lose electrons, and hence the net Pauli repulsion remains. Therefore, this HOMO−metal interaction dictates the U-dependence of Pauli

https://doi.org/10.1021/jacs.3c02447
J. Am. Chem. Soc. XXXX, XXX, XXX−XXX

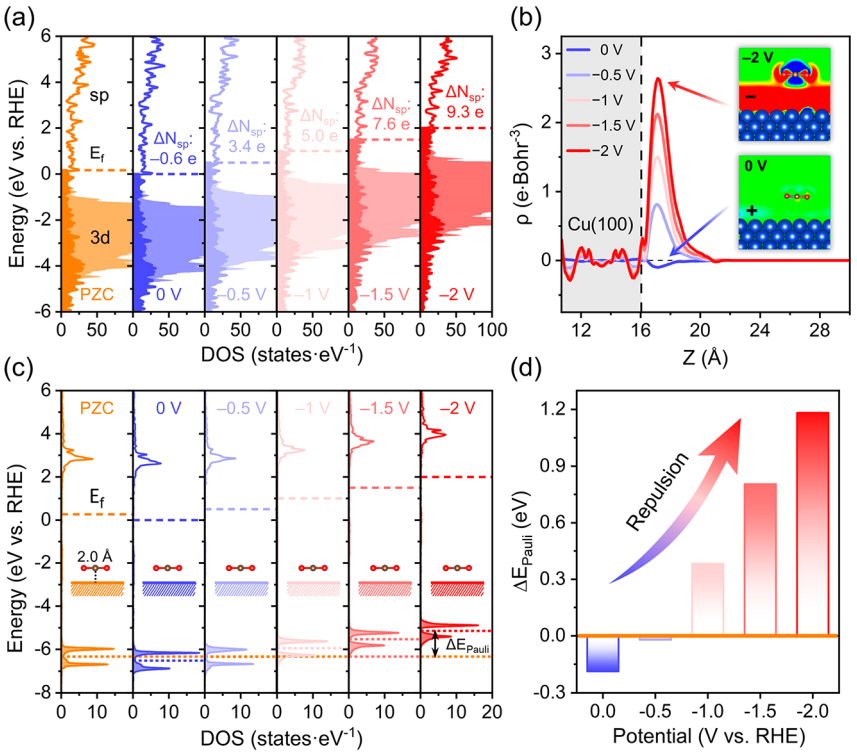

Figure 3. Quantitative analysis of the *U*-dependent Pauli repulsion in the physisorption PEC of CO_2 on Cu(100). (a) The partial DOSs (pDOSs) of the Cu(100) surface at U = PZC, 0 V, −0.5 V, −1 V, −1.5 V, and −2 V. ΔN_{sp} is the change in the number of electrons in the sp pDOS with respect to the PZC case, and ΔN_{sp} is very close to the corresponding changes in the total number of electrons (Table S5), so the electrons fill up mostly the sp pDOS of the Cu surface as U decreases. Note that all the energies are aligned by reference to the electrochemical potential of RHE. (b) The interfacial net charge densities on the Cu(100) surface relative to the PZC condition from 0 V to −2 V (the dashed line marks the surface). (c) The pDOSs of HOMOs and LUMOs of the linear CO_2 molecule fixed to be 2.0 Å above the Cu(100) surface, and the change of Pauli repulsion (ΔE_{Pauli}) is defined as the increase of the average position of HOMOs of CO_2 with respect to that at PZC. (d) ΔE_{Pauli} defined in (c) as a function of U from 0 V to −2 V.

repulsion in the physisorption PEC, which determines the *U*-dependence of the barrier and results in the inverted region. In order to confirm this understanding quantitatively, we further investigate the *U*-dependences of electronic structures.

Figure 3a shows the partial DOSs (pDOSs) of the Cu(100) surface at varying U from the potential of zero charge (PZC) to −2 V, and as U decreases, the sp pDOS of the Cu surface fills up significantly. This results in the drastically accumulating electron density at the Cu surface that extends more outward, as demonstrated in Figure 3b. Consequently, we investigate the pDOS of CO_2 with a frozen linear configuration and a fixed distance of 2 Å to the Cu(100) surface under varying U, as shown in Figure 3c. The frozen linear configuration rules out the chemical bonding between CO_2 and the Cu surface, i.e., the LUMO−metal interactions, and hence this scenario demonstrates mainly the HOMO−metal interactions that give rise to the Pauli repulsion and dominate the physisorption PEC. As U decreases, the electron density of the Cu surface extends more outward, and the HOMO−metal interactions are thus strengthened by the increasing overlaps. This leads to the continual rise of the HOMOs of CO_2 (split by the presence of surface) in energy, which can quantitatively characterize the increase in the Pauli repulsion (ΔE_{Pauli}). As shown in Figure 3c, we define and calculate ΔE_{Pauli} as the increase of the average position of HOMOs of CO_2 with respect to that at PZC, and Figure 3d demonstrates that ΔE_{Pauli} indeed grows significantly and monotonically with the decreasing U. Similar results and quantitative characterization of ΔE_{Pauli} can be found on Cu(111), as shown in Figure S4.

Therefore, we conclude that the inverted region in the CO_2 activation of eCO_2RR on Cu arises from the negative *U*-dependence of the Pauli repulsion in the physisorption PEC, which results from the HOMO−metal interactions rapidly strengthened by the accumulating electron density at the electrode surface. The presence of the inverted region jeopardizes the kinetics and thus the catalytic performance, and this in fact presents a strategy for designing better catalysts, i.e., to identify the catalyst designs that can suppress the Pauli repulsion and thus the inverted region. Accordingly, if the Pauli repulsion can be effectively lowered, as already explored in homogeneous catalysis,[59] the kinetics of CO_2 activation in eCO_2RR may be significantly promoted. We note that previous experimental studies have demonstrated that the Cu-based electrocatalysts rich in undercoordinated Cu sites deliver improved catalytic activities.[60−63] Thus, we further investigate the CO_2 activation on three distinctive types of Cu-based electrocatalysts with different coordination environments to explore for possible catalyst designs that can alleviate the effect of Pauli repulsion on the barrier of CO_2 activation in eCO_2RR.

The first type is the Cu(211) surface that has a step composed of less coordinated Cu sites, compared with Cu(100) and Cu(111), as shown in Figure 4a. The CO_2 activation occurs at the step of Cu(211), while the interfacial electron density on Cu(211) displays a wavy distribution in

https://doi.org/10.1021/jacs.3c02447
J. Am. Chem. Soc. XXXX, XXX, XXX−XXX

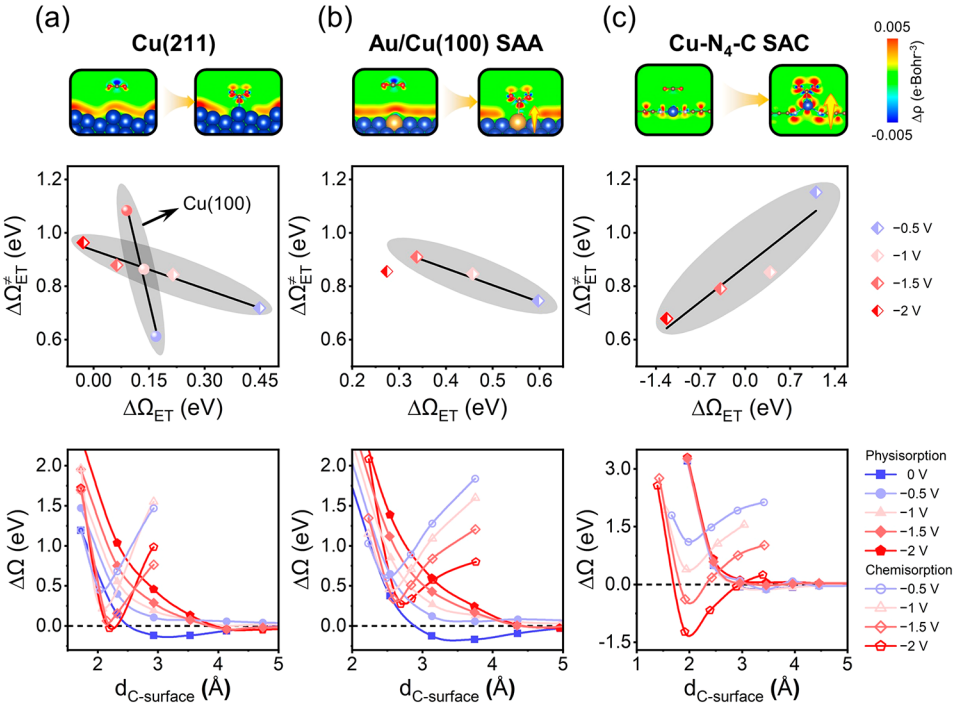

Figure 4. Designs of Cu-based electrocatalysts that can alleviate the effect of Pauli repulsion on the barrier of CO_2 activation in eCO_2RR. (a) The Cu(211) step surface, (b) the Au/Cu(100) single-atom alloy (SAA), and (c) the Cu single-atom catalyst (SAC) coordinated by four N atoms in the N-doped graphene (Cu-N_4-C). For each case, the top shows the interfacial net charge densities upon physisorption and chemisorption at U = −2 V relative to the PZC condition, the middle shows the correlation between $\Delta\Omega_{ET}^{\neq}$ and $\Delta\Omega_{ET}$ at varying U, and the bottom shows the physisorption and chemisorption PECs at varying U. Note that, at 0 V, the CO_2 molecule cannot form stable chemisorption on Au/Cu(100) SAA and Cu-N_4-C SAC, so there are no well-defined $\Delta\Omega_{ET}$ and $\Delta\Omega_{ET}^{\neq}$.

accordance with the rugged surface, and this leads to decreased overlaps for the HOMO−metal interactions, thus lowering the Pauli repulsion. Indeed, although an inverted region still exists for $\Delta\Omega_{ET}^{\neq}$ on Cu(211), it has a much weaker dependence on U than that on Cu(100), i.e., $\Delta\Omega_{ET}^{\neq}$ increases less significantly as U decreases. Figure 4a also shows the U-dependent physisorption PEC of CO_2 on Cu(211) that rises less rapidly as U decreases, and so does its crossing with the chemisorption PEC, which is consistent with the trend in the barrier. Therefore, increasing the surface roughness is an effective design for lowering the Pauli repulsion in eCO_2RR.

The second type is the Au/Cu(100) single-atom alloy (SAA) that has a single-atom Au site with flexible coordination to the Cu matrix, as shown in Figure 4b. The CO_2 activation occurs at the single-atom Au site, and its flexible coordination enables it to be pulled out of the surface to form the TS and the chemisorption (see also Figure S8). This flexibility of active site effectively lowers the Pauli repulsion, because it renders the CO_2 moiety in the TS and chemisorption further away from the Cu surface. Thus, the inverted region for $\Delta\Omega_{ET}^{\neq}$ on the Au/Cu(100) SAA has a weak dependence on U, similar to that on the Cu(211) step surface. The U-dependent crossings between the physisorption and chemisorption PECs shift to larger adsorption heights of CO_2, which embodies the flexibility of the active site to go out of the surface. Therefore, increasing the coordination flexibility of the active sites is another effective design for lowering the Pauli repulsion in eCO_2RR.

The third type is the Cu single-atom catalyst (SAC) coordinated by four N atoms in the N-doped graphene (Cu-N_4-C), as shown in Figure 4c. The graphene substrate in this Cu SAC shows much less significant interfacial electron accumulation (Figure S12), and this leads to the dramatic result that the physisorption PEC has little dependence on U; that is, the Pauli repulsion barely increases as U decreases, as shown at the bottom of Figure 4c. In addition, the Cu active site in this Cu SAC is also flexible and thus can go out of the catalyst surface to adopt the chemisorption of CO_2. The two factors combined completely eliminates the inverted region, and $\Delta\Omega_{ET}^{\neq}$ on Cu-N_4-C just follows a normal BEP relation. Therefore, the design of SAC on a substrate with less charging is effective to greatly suppress the Pauli repulsion. We note that recent studies have shown that the flexibility of the active site in SAC can lead to the potential-driven reconstruction of the active site in electrochemical reduction reactions such as eCO_2RR and ORR,[64−66] so there may be a subtle balance between the stability and the activity of SACs to consider.

Therefore, the fundamental understanding we formulated is likely to be generally applicable, and we can derive rational design strategies based on it. Besides the design of electrocatalysts, we note that the cations in the electrolyte may play a significant role in the kinetics of eCO_2RR through forming specific complexes with the chemisorbed CO_2.[19,67] This might be another effective strategy to alleviate the effect of Pauli repulsion on the kinetics of eCO_2RR, but we only include here the effect of cations in the implicit electrolyte model, neglecting their explicit coordination to CO_2, and we will investigate it explicitly in the future study. We also note that, in the kinetically unfavored CPET mechanism, there is also a small inverted region from −1 V to −1.5 V on Cu(100) (Table S2), with a much weaker dependence on U than that for the ET step in the SEPT mechanism. This implies that the Pauli repulsion also affects the kinetics of the CPET step, but to a very limited degree, and it may be alleviated by the proton of

https://doi.org/10.1021/jacs.3c02447
J. Am. Chem. Soc. XXXX, XXX, XXX−XXX

the water molecule, which is likely to play a similar role to that of cations.

Moreover, it is noteworthy that the kinetics of hydrogen evolution reaction (HER), which is the major competing reaction to eCO_2RR, can also be strongly influenced by the repulsion effects from the negatively charged electrodes at negative potentials. This arises from the fact that the reactant of HER is the interfacial water molecule in a wide pH range[68−71] or the bicarbonate anion via the bicarbonate reduction pathway in bicarbonate buffer,[72] and either the water molecule as a dipole or the bicarbonate anion experiences direct electrostatic repulsion from the negatively charged electrode, which consequently affects the subsequent transition state and thus the barrier.[68−72] In addition, the cations were found to promote the kinetics of HER possibly by lowering the electrostatic repulsion.[67,73−75] Nevertheless, there is an intrinsic difference between the scenarios in HER and eCO_2RR. The CO_2 molecule is nonpolar and neutral, so the repulsion it experiences from the negatively charged electrode is a quantum effect by the Pauli exclusion principle that results in the Pauli repulsion between fully occupied orbitals. The water molecule as the reactant of HER is also a closed-shell molecule, which should experience the Pauli repulsion in addition to the electrostatic repulsion, as embodied by the reorientation of the water molecule under the influence of negative potentials (Figure S13), which we will investigate in the future study.

CONCLUSION

To summarize, we have formulated a fundamental understanding of the interplay between the applied potential and the kinetics of CO_2 activation in eCO_2RR on Cu. First, we found that the nature of the CO_2 activation mechanism in eCO_2RR varies with U, and it is dominated by the SEPT mechanism at the common working U while switched to the CPET mechanism at highly negative U. Next, we identified inverted regions for $\Delta\Omega_{ET}^{\neq}$ in the SEPT mechanism of CO_2 activation that directly contradict the BEP relation, and the decreasing U does not instill the thermodynamic driving force into the kinetics but rather raises $\Delta\Omega_{ET}^{\neq}$ so high at highly negative U that the CO_2 activation has to switch to the CPET mechanism. We further demonstrated that the inverted region originates from the rapid rising of Pauli repulsion in the physisorption PEC as U decreases, and this is a result from the fact that the repulsive HOMO−metal interactions between CO_2 and Cu surfaces are greatly strengthened by the accumulating electron density at the electrode surface.

Finally, we showed that there are effective designs of electrocatalysts to suppress the adverse effect of Pauli repulsion on the kinetics of CO_2 activation in eCO_2RR, which include the increasing of the catalyst surface roughness, the introduction of flexible coordination of the active site, and the SAC on a substrate with less charging. Thus, the fundamental understanding formulated in this work provides novel insights into the rational design of highly efficient electrocatalysts for eCO_2RR, and moreover, it is likely to be generally applicable to the electrochemical reduction reactions of other closed-shell molecules including H_2O, CO, and N_2.

ASSOCIATED CONTENT

Supporting Information

The Supporting Information is available free of charge at https://pubs.acs.org/doi/10.1021/jacs.3c02447.

Additional computational details and supplemental tables (S1−S5) and figures (S1−S13) as noted in the text (PDF)

Coordinates of all structures (ZIP)

AUTHOR INFORMATION

Corresponding Author

Hai Xiao − *Department of Chemistry and Key Laboratory of Organic Optoelectronics and Molecular Engineering of Ministry of Education, Tsinghua University, Beijing 100084, China;* orcid.org/0000-0001-9399-1584; Email: haixiao@tsinghua.edu.cn

Author

Leyu Liu − *Department of Chemistry and Key Laboratory of Organic Optoelectronics and Molecular Engineering of Ministry of Education, Tsinghua University, Beijing 100084, China;* orcid.org/0009-0009-6703-6052

Complete contact information is available at: https://pubs.acs.org/10.1021/jacs.3c02447

Notes

The authors declare no competing financial interest.

ACKNOWLEDGMENTS

This work was supported by National Natural Science Foundation of China (Nos. 22122304 and 92261111), Tsinghua University Dushi Program, National Key Research and Development Project (2022YFA1503000), and Tsinghua University Initiative Scientific Research Program (20221080065). We are grateful to the Center of High-Performance Computing at Tsinghua University and Tsinghua Xuetang Talents Program for providing computational resources.

REFERENCES

(1) Ross, M. B.; De Luna, P.; Li, Y.; Dinh, C.-T.; Kim, D.; Yang, P.; Sargent, E. H. Designing materials for electrochemical carbon dioxide recycling. *Nat. Catal.* **2019**, *2* (8), 648−658.

(2) Chu, S.; Cui, Y.; Liu, N. The path towards sustainable energy. *Nat. Mater.* **2017**, *16* (1), 16−22.

(3) Zhong, M.; Tran, K.; Min, Y.; Wang, C.; Wang, Z.; Dinh, C.-T.; De Luna, P.; Yu, Z.; Rasouli, A. S.; Brodersen, P.; Sun, S.; Voznyy, O.; Tan, C.-S.; Askerka, M.; Che, F.; Liu, M.; Seifitokaldani, A.; Pang, Y.; Lo, S.-C.; Ip, A.; Ulissi, Z.; Sargent, E. H. Accelerated discovery of CO_2 electrocatalysts using active machine learning. *Nature* **2020**, *581* (7807), 178−183.

(4) Huang, J. E.; Li, F.; Ozden, A.; Sedighian Rasouli, A.; García de Arquer, F. P.; Liu, S.; Zhang, S.; Luo, M.; Wang, X.; Lum, Y.; Xu, Y.; Bertens, K.; Miao, R. K.; Dinh, C.-T.; Sinton, D.; Sargent, E. H. CO_2 electrolysis to multicarbon products in strong acid. *Science* **2021**, *372* (6546), 1074−1078.

(5) Dinh, C.-T.; Burdyny, T.; Kibria, M. G.; Seifitokaldani, A.; Gabardo, C. M.; García de Arquer, F. P.; Kiani, A.; Edwards, J. P.; De Luna, P.; Bushuyev, O. S.; Zou, C.; Quintero-Bermudez, R.; Pang, Y.; Sinton, D.; Sargent, E. H. CO_2 electroreduction to ethylene via hydroxide-mediated copper catalysis at an abrupt interface. *Science* **2018**, *360* (6390), 783−787.

(6) Xu, A.; Hung, S.-F.; Cao, A.; Wang, Z.; Karmodak, N.; Huang, J. E.; Yan, Y.; Sedighian Rasouli, A.; Ozden, A.; Wu, F.-Y.; Lin, Z.-Y.; Tsai, H.-J.; Lee, T.-J.; Li, F.; Luo, M.; Wang, Y.; Wang, X.; Abed, J.; Wang, Z.; Nam, D.-H.; Li, Y. C.; Ip, A. H.; Sinton, D.; Dong, C.; Sargent, E. H. Copper/alkaline earth metal oxide interfaces for electrochemical CO_2-to-alcohol conversion by selective hydrogenation. *Nat. Catal.* **2022**, *5* (12), 1081−1088.

(7) Ma, W.; Xie, S.; Liu, T.; Fan, Q.; Ye, J.; Sun, F.; Jiang, Z.; Zhang, Q.; Cheng, J.; Wang, Y. Electrocatalytic reduction of CO_2 to ethylene and ethanol through hydrogen-assisted C-C coupling over fluorine-modified copper. *Nat. Catal.* **2020**, *3* (6), 478−487.
(8) Li, F.; Thevenon, A.; Rosas-Hernandez, A.; Wang, Z.; Li, Y.; Gabardo, C. M.; Ozden, A.; Dinh, C. T.; Li, J.; Wang, Y.; Edwards, J. P.; Xu, Y.; McCallum, C.; Tao, L.; Liang, Z. Q.; Luo, M.; Wang, X.; Li, H.; O'Brien, C. P.; Tan, C. S.; Nam, D. H.; Quintero-Bermudez, R.; Zhuang, T. T.; Li, Y. C.; Han, Z.; Britt, R. D.; Sinton, D.; Agapie, T.; Peters, J. C.; Sargent, E. H. Molecular tuning of CO_2-to-ethylene conversion. *Nature* **2020**, *577* (7791), 509−513.
(9) Luc, W.; Fu, X.; Shi, J.; Lv, J.-J.; Jouny, M.; Ko, B. H.; Xu, Y.; Tu, Q.; Hu, X.; Wu, J.; Yue, Q.; Liu, Y.; Jiao, F.; Kang, Y. Two-dimensional copper nanosheets for electrochemical reduction of carbon monoxide to acetate. *Nat. Catal.* **2019**, *2* (5), 423−430.
(10) Chen, X.; Chen, J.; Alghoraibi, N. M.; Henckel, D. A.; Zhang, R.; Nwabara, U. O.; Madsen, K. E.; Kenis, P. J. A.; Zimmerman, S. C.; Gewirth, A. A. Electrochemical CO_2-to-ethylene conversion on polyamine-incorporated Cu electrodes. *Nat. Catal.* **2021**, *4* (1), 20−27.
(11) Ozden, A.; García De Arquer, F. P.; Huang, J. E.; Wicks, J.; Sisler, J.; Miao, R. K.; O'Brien, C. P.; Lee, G.; Wang, X.; Ip, A. H.; Sargent, E. H.; Sinton, D. Carbon-efficient carbon dioxide electrolysers. *Nat. Sustain.* **2022**, *5* (7), 563−573.
(12) Zhao, Y.; Zu, X.; Chen, R.; Li, X.; Jiang, Y.; Wang, Z.; Wang, S.; Wu, Y.; Sun, Y.; Xie, Y. Industrial-Current-Density CO_2-to-C_{2+} Electroreduction by Anti-swelling Anion-Exchange Ionomer-Modified Oxide-Derived Cu Nanosheets. *J. Am. Chem. Soc.* **2022**, *144* (23), 10446−10454.
(13) Jin, S.; Hao, Z.; Zhang, K.; Yan, Z.; Chen, J. Advances and Challenges for the Electrochemical Reduction of CO_2 to CO: From Fundamentals to Industrialization. *Angew. Chem., Int. Ed.* **2021**, *133* (38), 20795−20816.
(14) Nitopi, S.; Bertheussen, E.; Scott, S. B.; Liu, X.; Engstfeld, A. K.; Horch, S.; Seger, B.; Stephens, I. E. L.; Chan, K.; Hahn, C.; Nørskov, J. K.; Jaramillo, T. F.; Chorkendorff, I. Progress and Perspectives of Electrochemical CO_2 Reduction on Copper in Aqueous Electrolyte. *Chem. Rev.* **2019**, *119* (12), 7610−7672.
(15) Birdja, Y. Y.; Pérez-Gallent, E.; Figueiredo, M. C.; Göttle, A. J.; Calle-Vallejo, F.; Koper, M. T. M. Advances and challenges in understanding the electrocatalytic conversion of carbon dioxide to fuels. *Nat. Energy* **2019**, *4* (9), 732−745.
(16) Sun, Z.; Hu, Y.; Zhou, D.; Sun, M.; Wang, S.; Chen, W. Factors Influencing the Performance of Copper-Bearing Catalysts in the CO_2 Reduction System. *ACS Energy Lett.* **2021**, *6* (11), 3992−4022.
(17) Vijay, S.; Ju, W.; Brückner, S.; Tsang, S.-C.; Strasser, P.; Chan, K. Unified mechanistic understanding of CO_2 reduction to CO on transition metal and single atom catalysts. *Nat. Catal.* **2021**, *4* (12), 1024−1031.
(18) Qin, X.; Vegge, T.; Hansen, H. A. Cation-Coordinated Inner-Sphere CO_2 Electroreduction at Au-Water Interfaces. *J. Am. Chem. Soc.* **2023**, *145* (3), 1897−1905.
(19) Monteiro, M. C. O.; Dattila, F.; Hagedoorn, B.; García-Muelas, R.; López, N.; Koper, M. T. M. Absence of CO_2 electroreduction on copper, gold and silver electrodes without metal cations in solution. *Nat. Catal.* **2021**, *4* (8), 654−662.
(20) Xiao, H.; Goddard, W. A.; Cheng, T.; Liu, Y. Cu metal embedded in oxidized matrix catalyst to promote CO_2 activation and CO dimerization for electrochemical reduction of CO_2. *Proc. Natl. Acad. Sci. USA* **2017**, *114* (26), 6685−6688.
(21) Cheng, T.; Xiao, H.; Goddard, W. A. Reaction Mechanisms for the Electrochemical Reduction of CO_2 to CO and Formate on the Cu(100) Surface at 298 K from Quantum Mechanics Free Energy Calculations with Explicit Water. *J. Am. Chem. Soc.* **2016**, *138* (42), 13802−13805.
(22) Zhao, Y.; Zhang, X.-G.; Bodappa, N.; Yang, W.-M.; Liang, Q.; Radjenovica, P. M.; Wang, Y.-H.; Zhang, Y.-J.; Dong, J.-C.; Tian, Z.-Q.; Li, J.-F. Elucidating electrochemical CO_2 reduction reaction processes on Cu(hkl) single-crystal surfaces by in situ Raman spectroscopy. *Energy Environ. Sci.* **2022**, *15* (9), 3968−3977.
(23) Favaro, M.; Xiao, H.; Cheng, T.; Goddard, W. A.; Yano, J.; Crumlin, E. J. Subsurface oxide plays a critical role in CO_2 activation by Cu(111) surfaces to form chemisorbed CO_2, the first step in reduction of CO_2. *Proc. Natl. Acad. Sci. USA* **2017**, *114* (26), 6706−6711.
(24) Ye, Y.; Yang, H.; Qian, J.; Su, H.; Lee, K.-J.; Cheng, T.; Xiao, H.; Yano, J.; Goddard, W. A.; Crumlin, E. J. Dramatic differences in carbon dioxide adsorption and initial steps of reduction between silver and copper. *Nat. Commun.* **2019**, *10* (1), 1875.
(25) Zhao, Z.-J.; Liu, S.; Zha, S.; Cheng, D.; Studt, F.; Henkelman, G.; Gong, J. Theory-guided design of catalytic materials using scaling relationships and reactivity descriptors. *Nat. Rev. Mater.* **2019**, *4* (12), 792−804.
(26) Michaelides, A.; Liu, Z. P.; Zhang, C. J.; Alavi, A.; King, D. A.; Hu, P. Identification of General Linear Relationships between Activation Energies and Enthalpy Changes for Dissociation Reactions at Surfaces. *J. Am. Chem. Soc.* **2003**, *125* (13), 3704−3705.
(27) Bligaard, T.; Nørskov, J. K.; Dahl, S.; Matthiesen, J.; Christensen, C. H.; Sehested, J. The Brønsted-Evans-Polanyi relation and the volcano curve in heterogeneous catalysis. *J. Catal.* **2004**, *224* (1), 206−217.
(28) Marcus, R. A. Electron transfer reactions in chemistry. Theory and experiment. *Rev. Mod. Phys.* **1993**, *65* (3), 599−610.
(29) Bockris, J. O. M.; Nagy, Z. Symmetry factor and transfer coefficient. A source of confusion in electrode kinetics. *J. Chem. Educ.* **1973**, *50* (12), 839.
(30) Kim, D.; Shi, J.; Liu, Y. Substantial Impact of Charge on Electrochemical Reactions of Two-Dimensional Materials. *J. Am. Chem. Soc.* **2018**, *140* (29), 9127−9131.
(31) Schwarz, K.; Sundararaman, R. The electrochemical interface in first-principles calculations. *Surf. Sci. Rep.* **2020**, *75* (2), 100492−100519.
(32) Li, C. Y.; Le, J. B.; Wang, Y. H.; Chen, S.; Yang, Z. L.; Li, J. F.; Cheng, J.; Tian, Z. Q. In situ probing electrified interfacial water structures at atomically flat surfaces. *Nat. Mater.* **2019**, *18* (7), 697−701.
(33) Sutin, N. Theory of Electron Transfer Reactions: Insights and Hindsights. In *Progress in Inorganic Chemistry*; *Wiley*, 1983; pp 441−498.
(34) Bard, A. J.; Faulkner, L. R.; White, H. S. Kinetics of Electrode Reactions. In *Electrochemical Methods: Fundamentals and Applications*, 2nd ed.; John Wiley & Sons, 2001; pp 87−136.
(35) Perdew, J. P.; Burke, K.; Ernzerhof, M. Generalized Gradient Approximation Made Simple. *Phys. Rev. Lett.* **1996**, *77* (18), 3865−3868.
(36) Grimme, S.; Antony, J.; Ehrlich, S.; Krieg, H. A consistent and accurate ab initio parametrization of density functional dispersion correction (DFT-D) for the 94 elements H-Pu. *J. Chem. Phys.* **2010**, *132* (15), 154104.
(37) Hammer, B.; Hansen, L. B.; Nørskov, J. K. Improved adsorption energetics within density-functional theory using revised Perdew-Burke-Ernzerhof functionals. *Phys. Rev. B* **1999**, *59* (11), 7413−7421.
(38) Dion, M.; Rydberg, H.; Schroder, E.; Langreth, D. C.; Lundqvist, B. I. van der Waals density functional for general geometries. *Phys. Rev. Lett.* **2004**, *92* (24), 246401.
(39) Roman-Perez, G.; Soler, J. M. Efficient implementation of a van der Waals density functional: application to double-wall carbon nanotubes. *Phys. Rev. Lett.* **2009**, *103* (9), 096102.
(40) Klimeš, J.; Bowler, D. R.; Michaelides, A. Van der Waals density functionals applied to solids. *Phys. Rev. B* **2011**, *83* (19), 195131.
(41) Lee, K.; Murray, É. D.; Kong, L.; Lundqvist, B. I.; Langreth, D. C. Higher-accuracy van der Waals density functional. *Phys. Rev. B* **2010**, *82* (8), 081101.
(42) Wellendorff, J.; Lundgaard, K. T.; Møgelhøj, A.; Petzold, V.; Landis, D. D.; Nørskov, J. K.; Bligaard, T.; Jacobsen, K. W. Density functionals for surface science: Exchange-correlation model develop-

https://doi.org/10.1021/jacs.3c02447
J. Am. Chem. Soc. XXXX, XXX, XXX−XXX

ment with Bayesian error estimation. *Phys. Rev. B* **2012**, *85* (23), 235149.
(43) Sundararaman, R.; Goddard, W. A., 3rd The charge-asymmetric nonlocally determined local-electric (CANDLE) solvation model. *J. Chem. Phys.* **2015**, *142* (6), 064107.
(44) Sundararaman, R.; Letchworth-Weaver, K.; Schwarz, K. A.; Gunceler, D.; Ozhabes, Y.; Arias, T. A. JDFTx: software for joint density-functional theory. *SoftwareX* **2017**, *6*, 278−284.
(45) Nørskov, J. K.; Rossmeisl, J.; Logadottir, A.; Lindqvist, L.; Kitchin, J. R.; Bligaard, T.; Jónsson, H. Origin of the Overpotential for Oxygen Reduction at a Fuel-Cell Cathode. *J. Phys. Chem. B* **2004**, *108* (46), 17886−17892.
(46) Xiao, H.; Cheng, T.; Goddard, W. A.; Sundararaman, R. Mechanistic Explanation of the pH Dependence and Onset Potentials for Hydrocarbon Products from Electrochemical Reduction of CO on Cu (111). *J. Am. Chem. Soc.* **2016**, *138* (2), 483−486.
(47) Xiao, H.; Cheng, T.; Goddard, W. A. Atomistic Mechanisms Underlying Selectivities in C_1 and C_2 Products from Electrochemical Reduction of CO on Cu(111). *J. Am. Chem. Soc.* **2017**, *139* (1), 130−136.
(48) Xiao, H.; Shin, H.; Goddard, W. A. Synergy between Fe and Ni in the optimal performance of (Ni,Fe)OOH catalysts for the oxygen evolution reaction. *Proc. Natl. Acad. Sci. USA* **2018**, *115* (23), 5872−5877.
(49) Mathew, K.; Kolluru, V. S. C.; Mula, S.; Steinmann, S. N.; Hennig, R. G. Implicit self-consistent electrolyte model in plane-wave density-functional theory. *J. Chem. Phys.* **2019**, *151* (23), 234101.
(50) Lindgren, P.; Kastlunger, G.; Peterson, A. A. Scaled and Dynamic Optimizations of Nudged Elastic Bands. *J. Chem. Theory Comput.* **2019**, *15* (11), 5787−5793.
(51) Hjorth Larsen, A.; Jorgen Mortensen, J.; Blomqvist, J.; Castelli, I. E.; Christensen, R.; Dulak, M.; Friis, J.; Groves, M. N.; Hammer, B.; Hargus, C.; Hermes, E. D.; Jennings, P. C.; Bjerre Jensen, P.; Kermode, J.; Kitchin, J. R.; Leonhard Kolsbjerg, E.; Kubal, J.; Kaasbjerg, K.; Lysgaard, S.; Bergmann Maronsson, J.; Maxson, T.; Olsen, T.; Pastewka, L.; Peterson, A.; Rostgaard, C.; Schiotz, J.; Schutt, O.; Strange, M.; Thygesen, K. S.; Vegge, T.; Vilhelmsen, L.; Walter, M.; Zeng, Z.; Jacobsen, K. W. The atomic simulation environment-a Python library for working with atoms. *J. Phys.: Condens. Matter* **2017**, *29* (27), 273002.
(52) Liu, H.; Wang, Y.; Bowman, J. M. Vibrational analysis of an ice Ih model from 0 to 4000 cm^{-1} using the ab initio WHBB potential energy surface. *J. Phys. Chem. B* **2013**, *117* (34), 10046−52.
(53) Bertie, J. E.; Whalley, E. Optical Spectra of Orientationally Disordered Crystals. II. Infrared Spectrum of Ice Ih and Ice Ic from 360 to 50 cm^{-1}. *J. Chem. Phys.* **1967**, *46* (4), 1271−1284.
(54) Hoffmann, R. Barriers to Chemisorption. In *Solids and Surfaces: A Chemist's View of Bonding in Extended Structures*; John Wiley & Sons, 1991; pp 74−75.
(55) Huber, F.; Berwanger, J.; Polesya, S.; Mankovsky, S.; Ebert, H.; Giessibl, F. J. Chemical bond formation showing a transition from physisorption to chemisorption. *Science* **2019**, *366* (6462), 235−238.
(56) Magnussen, O. M.; Groß, A. Toward an Atomic-Scale Understanding of Electrochemical Interface Structure and Dynamics. *J. Am. Chem. Soc.* **2019**, *141* (12), 4777−4790.
(57) Groß, A.; Sakong, S. Ab Initio Simulations of Water/Metal Interfaces. *Chem. Rev.* **2022**, *122* (12), 10746−10776.
(58) Sakong, S.; Groß, A. Water structures on a Pt(111) electrode from ab initio molecular dynamic simulations for a variety of electrochemical conditions. *Phys. Chem. Chem. Phys.* **2020**, *22* (19), 10431−10437.
(59) Hamlin, T. A.; Bickelhaupt, F. M.; Fernández, I. The Pauli Repulsion-Lowering Concept in Catalysis. *Acc. Chem. Res.* **2021**, *54* (8), 1972−1981.
(60) Simon, G. H.; Kley, C. S.; Roldan Cuenya, B. Potential-Dependent Morphology of Copper Catalysts During CO_2 Electroreduction Revealed by In Situ Atomic Force Microscopy. *Angew. Chem., Int. Ed.* **2021**, *60* (5), 2561−2568.
(61) Li, C. W.; Kanan, M. W. CO_2 reduction at low overpotential on Cu electrodes resulting from the reduction of thick Cu_2O films. *J. Am. Chem. Soc.* **2012**, *134* (17), 7231−4.
(62) Li, C. W.; Ciston, J.; Kanan, M. W. Electroreduction of carbon monoxide to liquid fuel on oxide-derived nanocrystalline copper. *Nature* **2014**, *508* (7497), 504−7.
(63) Yang, Y.; Louisia, S.; Yu, S.; Jin, J.; Roh, I.; Chen, C.; Fonseca Guzman, M. V.; Feijóo, J.; Chen, P.-C.; Wang, H.; Pollock, C. J.; Huang, X.; Shao, Y.-T.; Wang, C.; Muller, D. A.; Abruña, H. D.; Yang, P. Operando studies reveal active Cu nanograins for CO_2 electroreduction. *Nature* **2023**, *614* (7947), 262−269.
(64) Yang, J.; Qi, H.; Li, A.; Liu, X.; Yang, X.; Zhang, S.; Zhao, Q.; Jiang, Q.; Su, Y.; Zhang, L.; Li, J. F.; Tian, Z. Q.; Liu, W.; Wang, A.; Zhang, T. Potential-Driven Restructuring of Cu Single Atoms to Nanoparticles for Boosting the Electrochemical Reduction of Nitrate to Ammonia. *J. Am. Chem. Soc.* **2022**, *144* (27), 12062−12071.
(65) Xing, G.; Tong, M.; Yu, P.; Wang, L.; Zhang, G.; Tian, C.; Fu, H. Reconstruction of Highly Dense Cu-N_4 Active Sites in Electrocatalytic Oxygen Reduction Characterized by Operando Synchrotron Radiation. *Angew. Chem., Int. Ed.* **2022**, *61* (40), No. e202211098.
(66) Bai, X.; Zhao, X.; Zhang, Y.; Ling, C.; Zhou, Y.; Wang, J.; Liu, Y. Dynamic Stability of Copper Single-Atom Catalysts under Working Conditions. *J. Am. Chem. Soc.* **2022**, *144* (37), 17140−17148.
(67) Monteiro, M. C. O.; Dattila, F.; López, N.; Koper, M. T. M. The Role of Cation Acidity on the Competition between Hydrogen Evolution and CO_2 Reduction on Gold Electrodes. *J. Am. Chem. Soc.* **2022**, *144* (4), 1589−1602.
(68) Ledezma-Yanez, I.; Wallace, W. D. Z.; Sebastián-Pascual, P.; Climent, V.; Feliu, J. M.; Koper, M. T. M. Interfacial water reorganization as a pH-dependent descriptor of the hydrogen evolution rate on platinum electrodes. *Nat. Energy* **2017**, *2* (4), 17031.
(69) Sarabia, F. J.; Sebastián-Pascual, P.; Koper, M. T. M.; Climent, V.; Feliu, J. M. Effect of the Interfacial Water Structure on the Hydrogen Evolution Reaction on Pt(111) Modified with Different Nickel Hydroxide Coverages in Alkaline Media. *ACS Appl. Mater. Interfaces* **2019**, *11* (1), 613−623.
(70) McCrum, I. T.; Koper, M. T. M. The role of adsorbed hydroxide in hydrogen evolution reaction kinetics on modified platinum. *Nat. Energy* **2020**, *5* (11), 891−899.
(71) Janik, M. J.; McCrum, I. T.; Koper, M. T. M. On the presence of surface bound hydroxyl species on polycrystalline Pt electrodes in the "hydrogen potential region" (0−0.4 V-RHE). *J. Catal.* **2018**, *367*, 332−337.
(72) Marcandalli, G.; Boterman, K.; Koper, M. T. M. Understanding hydrogen evolution reaction in bicarbonate buffer. *J. Catal.* **2022**, *405*, 346−354.
(73) Chen, X.; McCrum, I. T.; Schwarz, K. A.; Janik, M. J.; Koper, M. T. M. Co-adsorption of Cations as the Cause of the Apparent pH Dependence of Hydrogen Adsorption on a Stepped Platinum Single-Crystal Electrode. *Angew. Chem., Int. Ed.* **2017**, *56* (47), 15025−15029.
(74) Goyal, A.; Koper, M. T. M. The Interrelated Effect of Cations and Electrolyte pH on the Hydrogen Evolution Reaction on Gold Electrodes in Alkaline Media. *Angew. Chem., Int. Ed.* **2021**, *60* (24), 13452−13462.
(75) Monteiro, M. C. O.; Goyal, A.; Moerland, P.; Koper, M. T. M. Understanding Cation Trends for Hydrogen Evolution on Platinum and Gold Electrodes in Alkaline Media. *ACS Catal.* **2021**, *11* (23), 14328−14335.

https://doi.org/10.1021/jacs.3c02447
J. Am. Chem. Soc. XXXX, XXX, XXX−XXX